CrystEngComm

PAPER

View Article Online
View Journal | View Issue

Cite this: *CrystEngComm*, 2021, **23**, 8563

Two Co(II) complexes containing pyridylbenzimidazole ligands as chemosensors for the sensing of levofloxacin, acetylacetone, and Ni^{2+} with high selectivity and sensitivity†

Ming-Yue Wen, Li Ren and Guang-Hua Cui *

Received 21st September 2021,
Accepted 3rd November 2021

DOI: 10.1039/d1ce01271a

rsc.li/crystengcomm

Two new Co(II) coordination compounds, namely $[Co(L)_{0.5}(DCDPE)]_n$ (**1**) and $[Co(L)(npth)]_n{\cdot}nH_2O$ (**2**) (L = 1,1′-(1,6-hexanediyl)bis[2-(2-pyridyl)benzimidazole], H_2DCDPE = 4,4′-dicarboxydiphenyl ether, H_2npth = 3-nitrophthalic acid), were hydrothermally prepared and characterized. **1** presents a 2D layered **3,4L83** network, while **2** exhibits a dinuclear structure. Both complexes possess high pH stabilities in the range from 3 to 12. **1** and **2** can serve as fluorescence probes to sense acetylacetone (acac), levofloxacin (LEV), and Ni^{2+} with high quenching constants and low detection limits. The fluorescence sensing mechanisms of **1** and **2** are discussed in detail.

1. Introduction

Excessive organics, antibiotics and metal ions have given rise to serious environmental pollution and threats to human health.[1–4] Acetylacetone (acac) is an important intermediate in organic synthesis, which plays a key role in fine chemicals industry, especially in pharmaceuticals, perfumes and pesticides.[5] However, as a toxic substance, acac has irritating effects on human eyes and skin, causing poisoning accompanied by headache, nausea and vomiting.[6] Acac is supposed to a combustible and explosive material on account of its volatility and flammability nature, and can cause serious environmental problems.[7] Quinolone antibiotics are synthetic broad-spectrum antimicrobials.[8] Levofloxacin (LEV), as a quinolone antibiotic, had been extensively employed in the treatment of infectious disease.[9] However, the abuse of LEV leads to serious adverse reactions, such as gastrointestinal reactions, central nervous system toxicity, and mental disorders.[10] In addition, high Ni^{2+} concentrations in the environment through food chains result in human lung damage, kidney malfunction, gastrointestinal distress, pulmonary fibrosis, renal edema, skin dermatitis and cancer.[11,12] Traditional methods for the detection of acac/LEV/Ni^{2+} ions are usually subject to many restrictions, such as strict operating requirements and expensive equipments, and they are time-consuming.[13]

In recent years, some coordination compounds have been investigated as sensors for the detection of small molecules, antibiotics and metal cations,[14–18] which may provides a new method for the detection of acac/LEV/Ni^{2+}. Ma's group[19] successfully synthesized two Zn(II) coordination complexes based on 1,1′-(1,6-hexanediyl)bis[2-(2-pyridyl)-benzimidazole] (L), and the photoluminescent emissions signalled that the two complexes could be as promising fluorescence sensors. As we all know, organic N-containing ligands have significant impacts on the properties of ternary complexes. In addition, L ligands containing a pyridine group not only possess good coordination abilities, but also display flexible conformation and supramolecular recognition sites, which provides the possibility of constructing multidimensional coordination compounds.[20,21]

Herein, two new ternary fluorescent coordination compounds, $[Co(L)_{0.5}(DCDPE)]_n$ (**1**) and $[Co(L)(npth)]_n{\cdot}nH_2O$ (**2**) (H_2DCDPE = 4,4′-dicarboxydiphenyl ether, H_2npth = 3-nitrophthalic acid), were successfully synthesized. **1** and **2** behave with good thermal and chemical stabilities. The excellent fluorescence sensing performances of the two complexes for acac, LEV and Ni^{2+} are presented. The fluorescent quenching

College of Chemical Engineering, Hebei Key Laboratory for Environment Photocatalytic and Electrocatalytic Materials, North China University of Science and Technology, No. 21 Bohai Road, Caofeidian new-city, Tangshan, Hebei, 063210, P. R. China. E-mail: tscghua@126.com; Fax: +86 315 8805462; Tel: +86 315 8805460

† Electronic supplementary information (ESI) available. CCDC 2094211 and 2094213 contain the supplementary crystallographic data for **1** and **2**, respectively. For ESI and crystallographic data in CIF or other electronic format see DOI: 10.1039/d1ce01271a

mechanism of the coordination compounds was studied through density functional theory (DFT), Mott–Schottky and fluorescence spectra experiments.

2. Experimental

2.1. Synthesis of $[Co(L)_{0.5}(DCDPE)]_n$ (1)

A mixture of $Co(OAc)_2{\cdot}2H_2O$ (0.058 g, 0.1 mmol), H_2DCDPE (0.026 g, 0.1 mmol), L (0.047 g, 0.1 mmol), and distilled water (10 mL) was placed in a Teflon-lined reactor (25 mL), which was heated at 140 °C for 3 days and then gradually cooled to room temperature at a rate of 5 °C h^{-1}. Orange crystals of **1** were obtained. Yield: 45.4% based on L. Anal. calcd for $C_{29}H_{22}CoN_3O_5$ (Mr = 551.42) C, 63.16; H, 4.02; N, 7.62. Found: C, 64.50; H, 3.93; N, 8.58. IR (cm^{-1}) 1685 (s), 1600 (s), 1537 (w), 1488 (w), 1380 (s), 1303 (m), 1241 (m), 1160 (w), 1010 (w), 746 (m).

2.2. Synthesis of $[Co(L)(npth)]_n{\cdot}nH_2O$ (2)

The synthesis of **2** was similar to that of **1**, except that H_2-DCDPE was replaced by H_2npth (0.021 g, 0.1 mmol). Yield: 42.2% based on the L ligands. Calcd for $C_{76}H_{66}Co_2N_{14}O_{14}$ (Mr = 1517.28): C, 60.16; H, 4.38; N, 12.92%. Found: C, 58.89; H, 4.73; N, 14.35%. IR: 3400 (s), 1613 (s), 1523 (m), 1450 (m), 1351 (m), 1151 (w), 973 (w), 742 (m).

2.3. Fluorescence sensing

4 mg of ground powder of **1**/**2** were immersed in 4 mL of acac, DCM (dichloromethane), DMAC (*N*,*N*-dimethylacetamide), DMF (*N*,*N*-dimethylformamide), DMSO (dimethyl sulfoxide), EtOH (ethanol), FA (formaldehyde), MeCN (acetonitrile), MeOH (methanol), NMP (*N*-methyl pyrrolidone) or NB (*N*-butanol) to assess their abilities for sensing small organic molecules. Water was used in the place of organic solvents as the blank test. All suspensions were sonicated for 30 minutes before a fluorescence sensing test. Different concentrations of acac aqueous solutions also affect the fluorescence emission intensities; thence, samples of **1** and **2** were soaked in a series of 4 mL acac solutions (0 to 13.7 mM for **1** and 0 to 0.8 mM for **2**). In addition, 4 mg of powdered **1**/**2** were dropped into 4 mL of mixed solutions (5×10^{-4} M) containing acac and the other solvents to evaluate the sensing selectivity of **1** and **2**.

The above fluorescence sensing experiment methods are also applicable for **1** to detect LEV and for **2** to detect Ni^{2+}. The other antibiotics consist of enrofloxacin (ENR), sulfadiazine (SDZ), sulfamethazine (SMZ), sulfamethoxazole (SMX), metronidazole (MDZ), ornidazole (ODZ), ronidazole (RNZ), nitrofurazone (NZF), nitrofurantoin (NIT), norfloxacin (NOR), ciprofloxacin (CPFX), and tetracycline (TC), and the metal ions include Na^+, K^+, Mg^{2+}, Ca^{2+}, Sr^{2+}, Ba^{2+}, Co^{2+}, Ag^+, Hg^{2+}, Pb^{2+}, La^{3+}, Sm^{3+}, Eu^{3+}, Gd^{3+}, Tb^{3+}, and Er^{3+}.

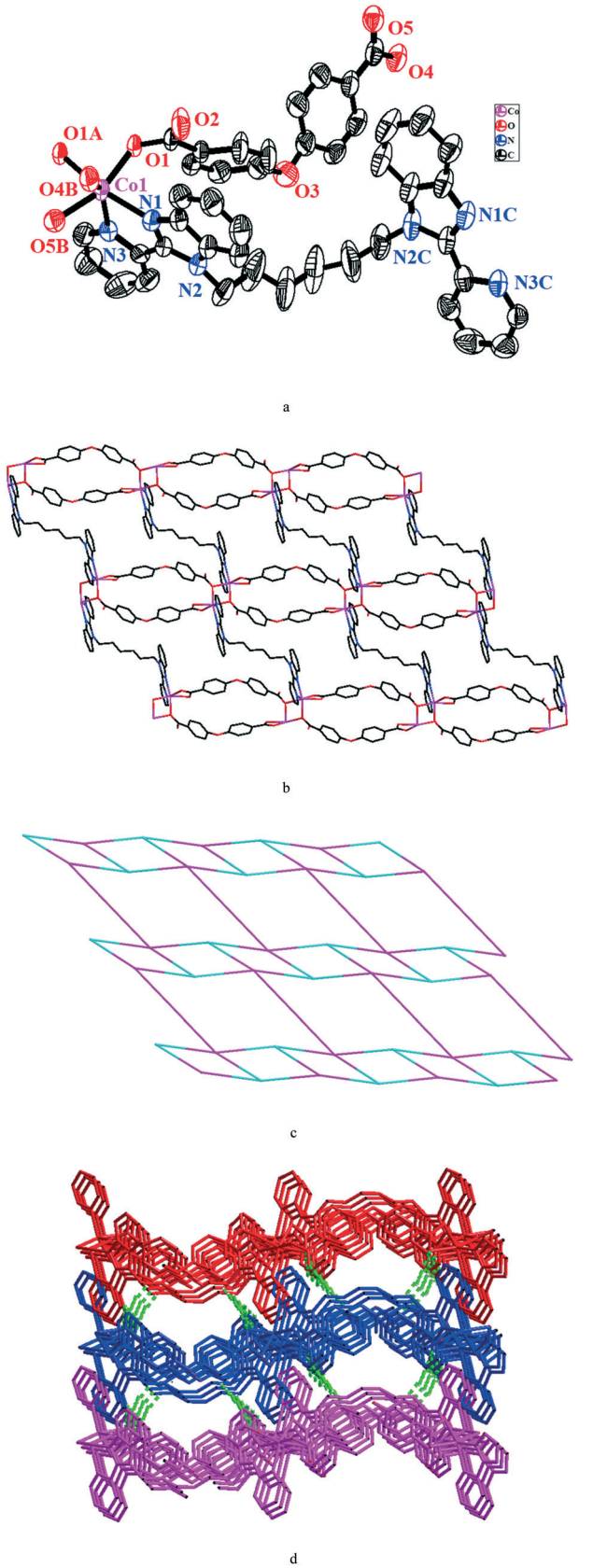

Fig. 1 a) The coordination environment of the Co(II) center in **1**. Symmetry codes: A: 1/2 − *x*, 3/2 − *y*, 1 − *z*; B: 1/2 + *x*, 3/2 − *y*, 1/2 + *z*; C: 1 − *x*, +*y*, 1/2 − *z*. b) The 2D network of **1**. c) The **3,4L83** topological network of **1**. d) The 3D network of **1** constructed *via* H-bonds.

3. Results and discussion

3.1. Crystal structure of $[Co(L)_{0.5}(DCDPE)]_n$ (1)

1 crystallizes in the monoclinic system, space group *C*2/*c*. There is a Co(II) center, a $DCDPE^{2-}$ ligand, and a half of L ligand in the asymmetric unit (Fig. 1a). Each Co(II) center adopts a distorted octahedral coordination geometry in which two nitrogen atoms (N1, N3) come from an L ligand, and four oxygen atoms (O1, O1A, O4B, O5B, symmetry code: A = 1/2 − *x*, 3/2 − *y*, 1 − *z*; B = 1/2 + *x*, 3/2 − *y*, 1/2 + *z*), come from three DCDPE ligands. The bond lengths of Co1–O/Co1–N are between 2.050(2) and 2.168 (4) Å, and 77.49(7)–167.07(10)° covers the bond angles around the Co(II) center, which is consistent with other Co(II) coordination compounds.[22–24]

In **1**, deprotonated $DCDPE^{2-}$ ligands bond to Co(II) centers by $(\kappa^1\text{-}\kappa^1)\text{-}(\kappa^2\text{-}\kappa^0)\text{-}\mu_3$ coordinating modes, shaping a 1D $[Co_2(DCDPE)_2]_n$ chain (Fig. S1†). The flexible L ligand connects adjacent Co(II) ions in a trans-conformation and further expands the 1D $[Co_2(DCDPE)_2]_n$ chains into the 2D layer (Fig. 1b); the dihedral angle between two benzimidazole rings is 26.493(2). From a topological point of view, Co(II) centers can be considered as 4-connected nodes, $DCDPE^{2-}$ anions act as 3-connected nodes and L ligands act as linkers. **1** presents a 2D **3,4L83** network with point symbol $\{4^2\cdot6^3\cdot8\}\{4^2\cdot6\}$ (Fig. 1c). The 2D network is further packed into a 3D supramolecular framework though weak hydrogen bonding interactions between the hydrogen atoms (H14 and H27A) of the L ligands and the neighbouring oxygen atoms (O2A, O5A) from the $DCDPE^{2-}$ [H14···O2A = 2.31(4) Å, H27A···O5A = 2.57(5) Å; C14–H14···O2A = 139(4)°, C27–H27A···O5A = 168 (5)°] (Fig. 1d).

3.2. Crystal structure of $[Co(L)(npth)]_n \cdot nH_2O$ (2)

2 belongs to the monoclinic system, $P2_1/n$ space group. The asymmetric unit contains a Co(II) center, an L ligand, a $npth^{2-}$ ligand, and a free H_2O molecule. As shown in Fig. 2a, the Co(II) center adopts a six-coordinated octahedral geometry $\{CoN_4O_2\}$ surrounded by two oxygen atoms (O2 and O4) and four nitrogen atoms (N3, N4, N6A, N7A, symmetry code: A = 1 − *x*, 1 − *y*, 1 − *z*), which come from one L ligand and two $npth^{2-}$ ligands, respectively. The range of bond distances of Co–O/N is 2.029(2)–2.178(2) Å, and the bond angles around the Co(II) center are in the range of 75.97(7)–170.67(7)°. All bond distances and angles are within the same normal ranges as **1**.

Two Co(II) centers are connected by two L ligands to give a dinuclear ring $[M_2L_2]$, and two $npth^{2-}$ ligands are attached to the sides of two Co(II) ions in the $(\kappa^1\text{-}\kappa^0)\text{-}(\kappa^1\text{-}\kappa^0)\text{-}\mu_1$ coordinating modes (Fig. 2b); the distance Co···Co is 12.154(9) Å. Firstly, the dinuclear structure can further extend in a plane by weak hydrogen bonding interactions between the hydrogen atoms (H4) of the L ligand and the neighbouring oxygen atoms (O3A) of a carboxyl group from the npth anions [H4···O3A = 2.56(3) Å,]; simultaneously, the weak hydrogen bonds between the oxygen atoms (O3A) of the $npth^{2-}$ and the adjacent hydrogen atoms (H38) of the L ligand enable the dinuclear ring to spread in another cross-linked plane. Ultimately, the dinuclear ring grows into a 3D supramolecular network. Fig. 2c and d are views of the 3D supramolecular framework in the *a*-axis and *b*-axis directions, respectively.

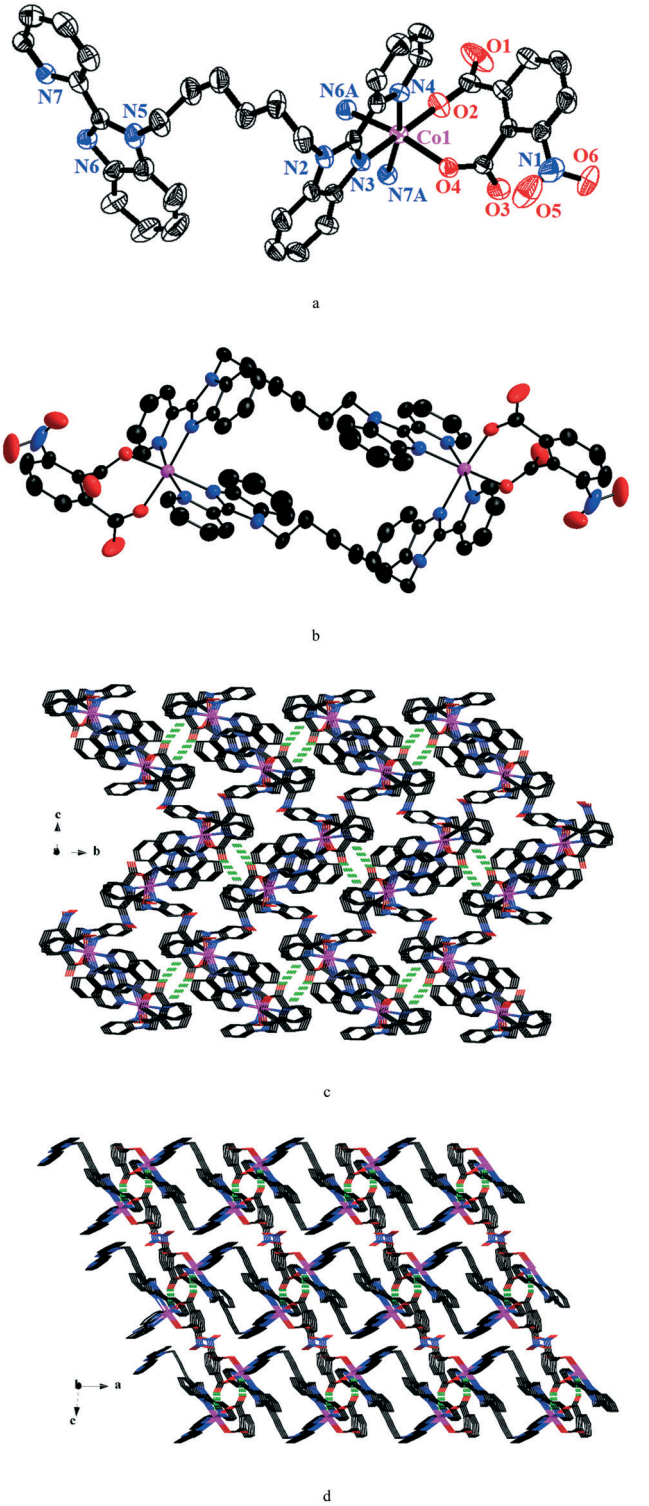

Fig. 2 a) The coordination environment centered on the Co(II) center in **2**; symmetry codes: A: 1 − *x*, 1 − *y*, 1 − *z*; B: 3/2 − *x*, 1/2 + *y*, 3/2 − *z*; C: 2 − *x*, 2 − *y*, 1 − *z*. b) A view of the dinuclear structure of **2**. c) The 3D network of **2** constructed *via* H-bonds in the *a*-axis direction. d) The 3D network of **2** constructed *via* H-bonds in the *b*-axis direction.

Table 1 The structural properties of the two complexes obtained using Poreblazer software

Property	1	2
Pore limiting diameter (Å)	1.40	1.37
Largest cavity dimeter (Å)	3.96	2.74
Accessible surface area ($m^2\ g^{-1}$)		
Probe-occupiable volume ($cm^3\ g^{-1}$)	0.206	0.171

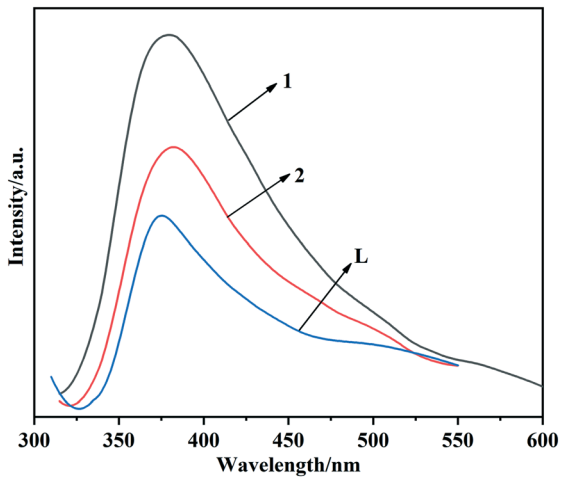

Fig. 3 Solid fluorescence spectra of the L ligand, **1**, and **2**.

3.3. IR and TGA

As illustrated in Fig. S2,† the IR spectrum of **2** shows a strong absorption peak near 3400 cm^{-1} corresponding to the vibration of water molecules. There was no strong absorption band around 1700 cm^{-1} in **1** or **2**, indicating that the –COOH groups in the $DCDPE^{2-}$ and $npth^{2-}$ ligands were completely deprotonated. The asymmetrical and symmetrical vibrations of the carboxyl group correspond to the peaks at 1685, 1630, and 1384 cm^{-1} for **1**, and 1612 and 1353 cm^{-1} for **2**. The values of $\Delta\nu[\nu_{as}(COO)-\nu_s(COO)]$ bands show that the carboxyl groups display monodentate ($\Delta\nu$ = 246 cm^{-1} for **1**, 259 cm^{-1} for **2**) and chelate ($\Delta\nu$ = 55 cm^{-1} for **2**) coordination modes. In addition, the stretching vibration bands of C=N form bis(benzimidazole) ligands can be found at 1535 cm^{-1} for **1** and 1526 cm^{-1} for **2**, respectively.

The TGA results of the two complexes are shown in Fig. S3.† There are two weight losses in the decomposition of **1**. The first decrease (41.7%, calcd 42.9%) occurs at 243 °C owing to the collapse of L ligands and lasts until 410 °C. The second one is sustained at 411–683 °C, which is ascribed to the release of $DCDPE^{2-}$ ligands (obsd 45.2%; calcd 46.4%). In **2**, the observed weight loss (obsd 3.2% and calcd 2.4%) occurs in the temperature range of 150–221 °C corresponding to the volatilization of H_2O molecules. In the temperature range of 221–488 °C, the removal of L ligands causes 57.2% (calcd 59.3%) weight loss of **2**. The weight continues to

Table 2 Computed isodensity surfaces of HOMO and LUMO orbitals of L, H_2DCDPE, H_2npth, and Co^{2+}

Organic molecule	HOMO	LUMO
L	−5.679 eV	−1.273 eV
H_2DCDPE	−6.625 eV	−1.651 eV
H_2npth	−7.511 eV	−2.793 eV
Co^{2+}	−10.353 eV	−2.496 eV

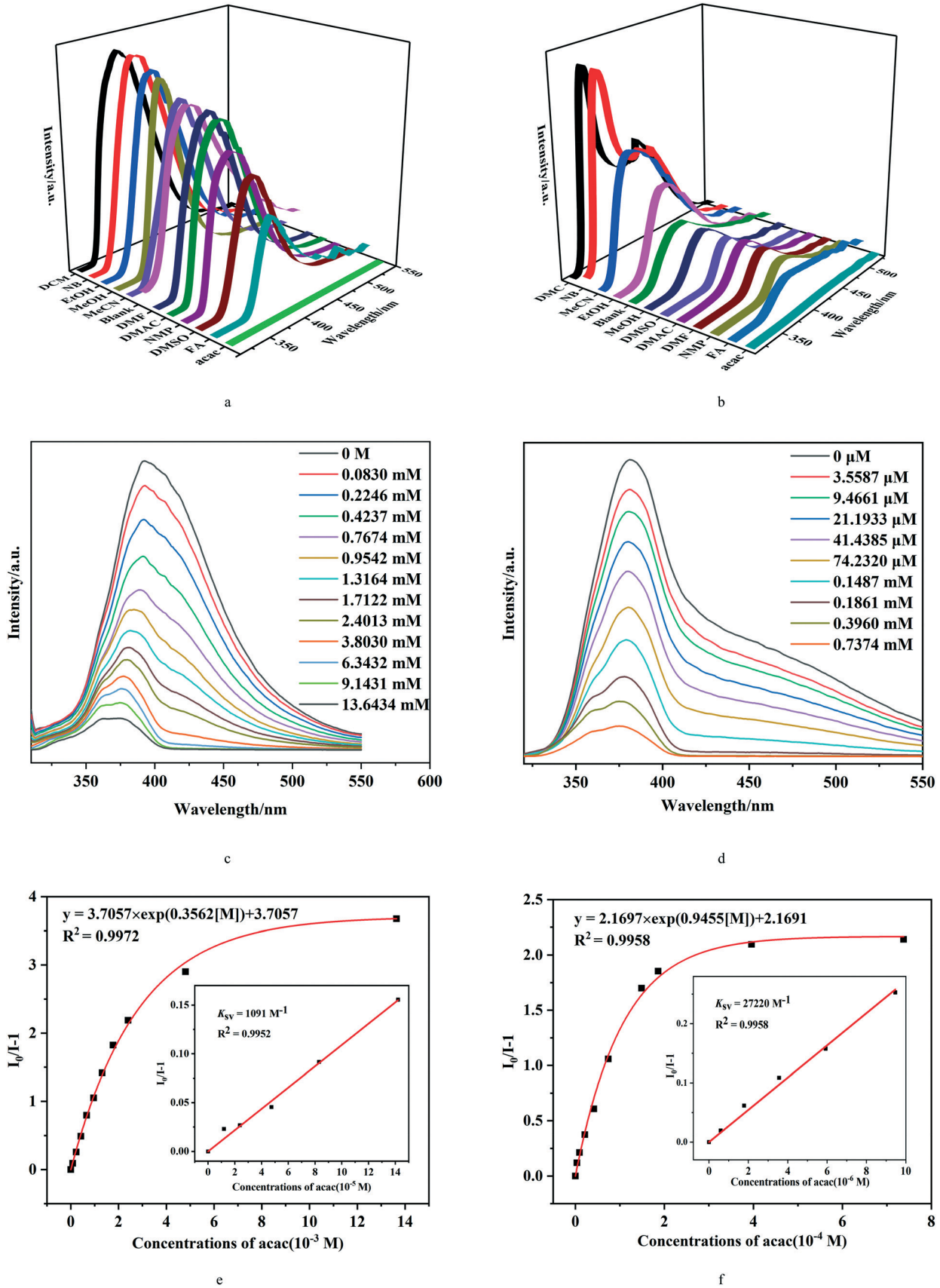

Fig. 4 Emission spectra of a) **1** and b) **2** in different organic solvents at room temperature. Fluorescence emission intensities at different concentrations of acac in c) **1** and d) **2**. The relationships between the emission intensities of e) **1** and f) **2** and the concentration of acac; insets: Stern–Volmer plots of I_0/I *vs.* [acac].

reduce by 30.9% (calcd 27.83%) between 448 and 649 °C, which is derived from the release of $npth^{2-}$ ligands. Finally, CoO remnants are left. Thus, **1** and **2** present highly thermal stabilities.

3.4. Powder X-ray diffraction and pH stability studies

The experimental PXRD patterns of **1** and **2** are consistent with those simulated from single-crystal data (Fig. S4†), illustrating that the samples have high-phase purity. The different reflection intensities may be owing to the variation in preferred orientation of the powder samples (Table 1).

As-prepared samples of **1**/**2** (4 mg) were soaked in solutions with different pH varying from 2 to 13, and the fluorescence was measured after 30 minutes of sonication. The results show that **1** and **2** possess excellent pH stabilities in the range from 3 to 12 (Fig. S5†). The chemical stability of **1** and **2** may be attributed to the hydrophobic groups of their L ligand (benzene ring; $-CH_2-$ group, *etc.*), smaller pore diameters and combined mixed donor linkers (hybrid N, O donor ligand).

3.5. Fluorescence and the sensing properties of two complexes

3.5.1 Fluorescence spectra. The luminescence properties of **1** and **2** as well as the free L ligands were investigated in the solid state at room temperature (Fig. 3). Their maximum emission wavelengths are 378 nm (λ_{ex} = 298 nm) for **1**, 381 nm (λ_{ex} = 299 nm) for **2** and 371 nm (λ_{ex} = 297 nm) for the L ligands. Compared with the L ligands, **1** and **2** show blue-shifts of 7 nm and 10 nm, respectively. The **1**, **2** and L ligands were dispersed in aqueous solution and measured 10 times in 100 min, the fluorescence intensities remained unchanged, indicating that **1**, **2** and L ligands were stable in aqueous solution (Fig. S6 and S7†). As a consequence, the shifts are not contingent. The lowest unoccupied molecular orbital (LUMO) energies of Co^{2+} ions, free L ligands, DCDPE and H_2npth ligands can be calculated by density functional theory (DFT).[25] The LUMOs of L ligands are located on benzimidazoles, while those of H_2DCDPE and the H_2npth ligand are located on carboxyl and nitro groups, respectively (Table 2).[26] Notably, the LUMO energies of the two ligands in **1** (−1.273 eV for L, −1.651 eV for H_2DCDPE) are higher than the counterpart, −2.496 eV, of Co^{2+} ions. Therefore, there is a greater possibility that the charge transfer from benzimidazoles of L and the carboxyl group of H_2DCDPE to Co^{2+} ions affects the blue-shift (LMCT).[27] For **2**, the LUMO energy of L is higher than that of Co^{2+} ions, while H_2npth (−2.793 eV) is lower than Co^{2+} ions, which implies that the charge transfer from the L ligand to the Co^{2+} ions and from Co^{2+} ions to H_2npth together cause the blue shift (LMCT and MLCT).[28]

3.5.2 Sensing of small organic molecules. The organic solvents behave with different degrees of quenching for **1** and **2** (Fig. 4a and b). **1** and **2** indicated sharp quenching (99.99% for **1** and 94.89% for **2**) in acac solvents, while the fluorescence properties of **1** and **2** were hardly changed by the other solvents. In addition, when other solvents were separately added to systems containing acac, the luminescent results illustrate that **1** and **2** were still quenched visibly by acac. Thus, **1** and **2** have excellent detection capabilities toward acac in mixed solutions (Fig. S8†).

The fluorescence intensities of **1** and **2** are inversely proportional to acac concentration (Fig. 4c and d). The quenching behaviors of acac can be fitted to $y = 3.7057\exp(0.3562\,[M]) + 3.7057$ for **1** (R^2 = 0.9972) and $y = 2.1697\exp(0.9455\,[M]) + 2.1691$ for **2** (R^2 = 0.9958 for **2**) (Fig. 4c and d). As shown in Fig. 4e and f, there are good linear relationships between the quenching effects and the acac concentration which is at low concentration (0–140 μM for **1** and 0–10 μM for **2**). The linear correlation equations were $I_0/I - 1 = 1091\,[acac] + 1$ and $I_0/I - 1 = 2.72 \times 10^4\,[acac]$ (R^2 = 0.9952 for **1** and R^2 = 0.9958 for **2**). The K_{sv} values were calculated to be 1.09×10^3 M^{-1} and 2.72×10^4 M^{-1} for **1** and **2**, respectively, using linear regression of the plots. The detection limits for acac were 1.76×10^{-5} M for **1** and 2.97×10^{-6} M for **2**, according to $3\sigma/k$ (σ: standard error; k: slope). This is comparable to the sensitivity of other coordination compounds for the sensing of acac (Table 3).[13,29]

3.5.3 Sensing of quinolone antibiotics. Observably, most of the antibiotics exert subtle effects on the fluorescent emission of **1**, while its intensity undergoes striking quenching by the introduction of LEV (Fig. 5a). The fluorescence intensities of **1** changed with different LEV concentrations. As the concentrations of LEV increased, the fluorescence intensities of **1** decreased gradually (Fig. 5b). The quenching behavior can be fitted to $y = 8.6211\exp(0.0350[M]) + 8.6394$ (R^2 = 0.9988). In addition, there is a good linear correlation (R^2 = 0.9918) between quenching efficiency and low concentrations of LEV (0–0.3 μM) with a K_{sv} value of 9.99×10^5 M^{-1} (Fig. 5c), and the LOD was 0.76 μM. Among the similar coordination compounds for detecting LEV, **1** displays a high sensitivity for detecting LEV (Table 4).[8,10,30] In addition, anti-interference experiments elucidate that **1** possesses a promising selectivity towards LEV even with the coexistence of other antibiotics (Fig. S9†).

3.5.4 Sensing of Ni^{2+} ions. The fluorescence intensities of **2** are highly affected by diverse metal ions, as can be seen in Fig. 5d. Ni^{2+} ions aroused substantial quenching (92.87%) for the fluorescence intensities of **2** among all metal ions. When

Table 3 A comparison of the sensitivities of **1** and **2** toward acac with related complexes

Complex	LOD/M	Ref.
$[Cd(L1)(DCTP)]_n$	9.57×10^{-6}	13
$[Cd(L2)(TPA)]_n$	1.61×10^{-7}	13
$[Zn_2(L3)(DCTP)_{1.5}(OH)]_n$	1.37×10^{-7}	29
1	1.76×10^{-7}	This work
2	2.97×10^{-6}	This work

L1 = 1,3-bis(5,6-dimethylbenzimidazol-1-yl)propane, L2 = 1,4-bis(5,6-dimethylbenzimidazol-1-yl)-2-butylene, H_2DCTP = 2,5-dichloroterephthalic acid, H_2TPA = terephthalic acid, L3 = 1,3-bis(5,6-methylbenzimidazol-1-yl) propane.

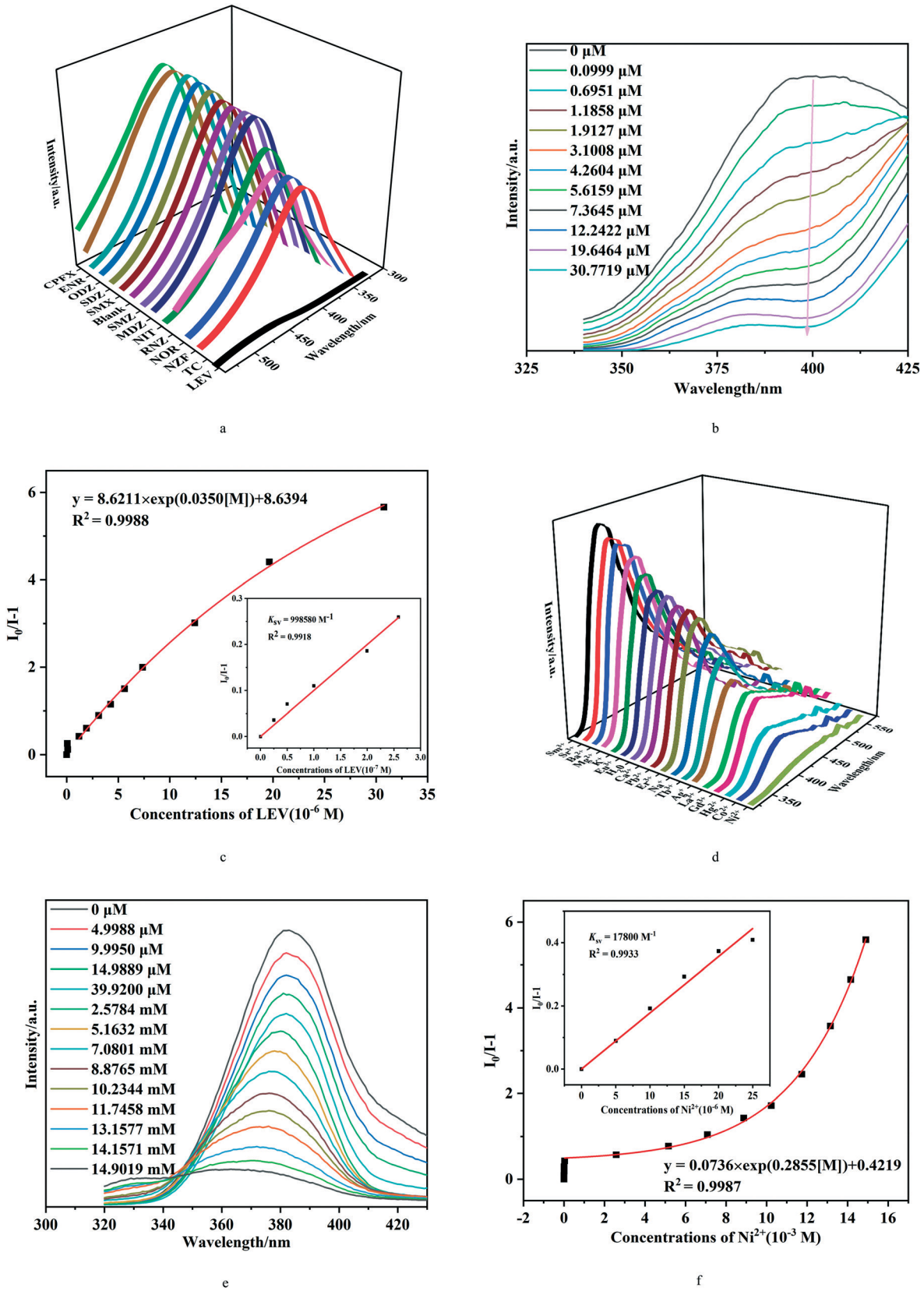

Fig. 5 a) Fluorescence emission spectra of **1** in different quinolone solutions with a concentration of 1×10^{-5} M at room temperature. b) Fluorescence emission spectra of **1** in water with different concentrations of LEV. c) The relationship between the emission intensity of **1** and the concentration of LEV; inset: Stern–Volmer plot of I_0/I *vs.* [LEV]. d) Fluorescence emission spectra of **2** in different metal solutions with a concentration of 1×10^{-5} M at room temperature. e) Fluorescence emission spectra of **2** in water with different concentrations of Ni^{2+}. f) The relationship between the emission intensity of **2** and the concentration of Ni^{2+}; inset: Stern–Volmer plot of I_0/I *vs.* [Ni^{2+}].

Table 4 A comparison of the sensitivity of **1** toward LEV with previously reported complexes

Complex	LOD/M	Ref
CdTe QDs	4.23×10^{-9}	8
Tb@TFP-EB	1.26×10^{-6}	10
$[Na_4CB[6](H_2O)_{10}(DMF)]\cdot 2BPDS\cdot 2H_2O$	1.60×10^{-7}	30
2	4.54×10^{-6}	This work

QDs = quantum dots, CB[6] = cucurbit[6]uril, H_2BPDS = 4,4′-biphenyldisulphonic acid, TFP = 2,4,6-trihydroxy-benzene-1,3,5-tricarbaldehyde, EB = ethidium bromide.

the Ni^{2+} ion concentrations were increased to 1.40×10^{-4} M, the fluorescence intensities of **2** declined gradually (Fig. 5e), and the quenching behavior can be fitted to $y = 0.0736 \exp(0.2855\ [M]) + 0.4219$ ($R^2 = 0.9987$). In addition, the Stern–Volmer curve for Ni^{2+} presents good linear correlation ($R^2 = 0.9933$) when the Ni^{2+} ions are at low concentration (0–25 μM) with calculated K_{sv} values of 1.78×10^4 M^{-1} (Fig. 5f), and the LOD is 4.54 μM. Meanwhile, **2** exhibits high sensitivity for the detection of Ni^{2+} ions compared with previously reported coordination compounds for sensing Ni^{2+} (Table 5).[18,31] Meanwhile, the quenching effect of Ni^{2+} is not interfered with the other metal ions, and **2** behaves with excellent selectivity for Ni^{2+} (Fig. S10†).

3.5.5 Fluorescence lifetime and dynamic quenching process. The fluorescence lifetime is obtained by a bi-exponential fit of the fluorescence decay data using formula 3 (Fig. S11 and S12†) and the average fluorescence lifetime is calculated using formula 4. The emission decay lifetimes for **1** and **2** were 1.737 and 3.837 μs, respectively. The shorter fluorescence lifetimes of **1** and **2** may have been caused by a contribution from a competitive nonradiative decay process in **1**/**2**.[32] Suitable acac and LEV (1×10^{-5} M) were added to powdered **1**, acac and Ni^{2+} (5×10^{-4} M) to **2**, respectively. The solid-state decay curves of **1** with acac and LEV and of **2** with acac and Ni^{2+} show different attenuation trends, which correspond to a dynamic quenching mechanism, while the immobile fluorescence lifetime denotes a static quenching process.[33]

3.5.6 The mechanism of sensing. To rationalize the possibility of quenching acac, LEV and Ni^{2+}, Mott–Schottky measurements of the complex samples were monitored at 1000, 1500 and 2000 Hz, respectively (Fig. 6). The positive slope is in accordance with an n-type semiconductor. The result demonstrates that $E_{cb} = -1.051$ eV for **1**, and $E_{cb} = -1.087$ eV for **2**. When Ag/AgCl serves as the reference surface, the lowest unoccupied molecular orbitals (LUMOs) of **1** and **2** were calculated to be −0.8286 eV *versus* Ag/AgCl and −0.8646 eV *versus* Ag/AgCl, respectively.[34] The LUMO level of **1** (−0.8286 eV) does lie higher than that of acac (−2.36 eV)[35] or LEV (−1.71 eV),[36] and the LUMO level of **2** (−0.8646 eV) is also higher than that of acac (−2.36 eV) or Ni^{2+} (−2.871 eV).[37] Thus, the quenching may be attributed to photo-induced electron transfer (PET) from the LUMOs of **1** and **2** to the LUMOs of acac, LEV and Ni^{2+} ions.[38]

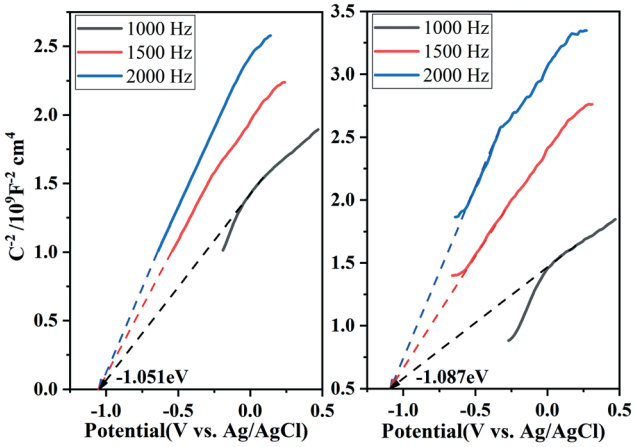

Fig. 6 Mott–Schottky plots for as-prepared (left) **1** and (right) **2** in 1 M Na_2SO_4 aqueous solution.

Table 5 A comparison of the sensitivity of **2** toward Ni^{2+} ions with previously reported complexes

Complex	LOD/M	Ref.
$[Eu(ADA)_{1.5}(phen)]_n$	1.00×10^{-9}	18
$[Co_2(LNPTA)(H_2O)]_n$	1.40×10^{-6}	31
2	4.54×10^{-6}	This work

phen = 1,10-phenanthroline, ADA = 1,3-adamantanediacetic acid, L = 1,2-bis(thiabendazole-1-ylmethyl)benzene, H_2NPTA = 2-nitroterephthalic acid.

On the other hand, the fluorescence quenching of **1** and **2** by acac/LEV/Ni^{2+} might result from the collapse of the framework and competitive absorption of energy.[39] There is no major difference in the PXRD patterns of **1** and **2** after sensing acac/LEV/Ni^{2+}, which reveals that the framework remains stable during the sensing process (Fig. S13†). It can be seen from Fig. S14–S16† that the excitation band of **1** overlaps with the absorption peaks of acac and LEV, and the excitation band of **2** overlaps with the absorption peaks of acac and Ni^{2+} as well. Hence, it can be inferred that there is competitive absorption of energy between the L ligands and acac, LEV and Ni^{2+}.[40] However, no overlap was observed for other organic molecules, metal cations or antibiotics. Consequently, the fluorescence quenching is caused by PET from **1**/**2** to the analyte molecules and the competitive absorption of the excitation light between **1**/**2** and the analyte molecule.

4. Conclusions

In conclusion, two Co(II)-based complexes were synthesized under hydrothermal conditions and characterized. **1** and **2** feature a 2D **3,4L83** framework and binuclear structure, respectively. The fluorescence sensing experiments confirm that **1** and **2** are promising sensors to detect acac and LEV (**1**), and acac and Ni^{2+} ions (**2**), with high selectivity, high sensitivity, and low detection limits. Both **1** and **2** exhibit high thermal and chemical stability.

Author contributions

Ming-Yue Wen: methodology, formal analysis, investigation, writing-original draft, data curation. Li Ren: software, visualization. Guang-Hua Cui: conceptualization, writing-review & editing, supervision, project administration, funding acquisition.

Conflicts of interest

The authors declare no conflicts of interest.

Acknowledgements

The project was supported by the Natural Science Foundation-Steel and Iron Foundation of Hebei Province (B2021209020).

References

1 G. Chakraborty, P. Das and S. K. Mandal, *ACS Appl. Mater. Interfaces*, 2020, **12**, 11724–11736.
2 A. L. Li, Y. H. Qu, L. Fu, C. Han and G. H. Cui, *CrystEngComm*, 2020, **22**, 2656–2666.
3 H. Zhu, L. Fu, D. Liu, Y. H. Li and G. Y. Dong, *J. Solid State Chem.*, 2020, **286**, 121265.
4 V. Verma and K. Arora, *Int. Pharm. Sci.*, 2021, **12**, 114.
5 B. M. Trost and M. C. Ryan, *Angew. Chem., Int. Ed.*, 2017, **56**, 2862–2879.
6 J. N. Cui, H. Zhu and G. H. Cui, *Inorg. Chem. Commun.*, 2021, **129**, 108654.
7 M. M. Fu, L. Fu and G. H. Cui, *Dalton Trans.*, 2021, **50**, 10180.
8 X. Tan, Q. Li and J. Yang, *J. Mol. Struct.*, 2020, **1201**, 127175.
9 P. Raja Lakshmi, P. Nanjan, S. Kannan and S. Shanmugaraju, *Coord. Chem. Rev.*, 2021, **435**, 213793.
10 X. Liang, H. Liu, Y. Du, W. Li, M. Wang, B. Ge and L. Zhao, *Colloids Surf., A*, 2020, **606**, 125429.
11 T. K. Grimsrud, S. R. Berge, T. Haldorsen and A. Andersen, *Am. J. Epidemiol.*, 2002, **156**, 1123–1132.
12 N. Ruecha, N. Soatthiyanon, C. Aumnate, Y. Boonyongmaneerat and N. Rodthongkum, *Cellul. Chem. Technol.*, 2020, **27**, 5211–5222.
13 M. Y. Wen, S. C. Wang, D. Liu and G. Y. Dong, *J. Solid State Chem.*, 2021, **1244**, 130954.
14 D. Men, S. Feng, G. Liu, L. Hang and T. Zhang, *Part. Part. Syst. Charact.*, 2020, **37**, 1900452.
15 J. H. Qin, P. Xu, Y.-D. Huang, L.-Y. Xiao, W. Lu, X.-G. Yang, L. Ma and S.-Q. Zang, *Chem. Commun.*, 2021, **57**, 8468–8471.
16 H. Fu, L. Yan, N. Wu, L. Ma and S. Zang, *J. Mater. Chem. A*, 2018, **6**, 9183–9191.
17 X. X. Wu, H. R. Fu, M. L. Han, Z. Zhou and L. F. Ma, *Cryst. Growth Des.*, 2017, **17**, 6041–6048.
18 G. L. Yang, X. L. Jiang, H. Xu and B. Zhao, *Small*, 2021, **17**, e2005327.
19 H. Y. Liu, H. Wu, J. F. Ma, Y. Y. Liu, B. Liu and J. Yang, *Cryst. Growth Des.*, 2010, **10**, 4795–4805.
20 G. Liu, S. Han, Y. Gao, N. Xu, X. Wang and B. Chen, *CrystEngComm*, 2020, **22**, 7952–7961.
21 S. Ghodke, A. Tamboli, A. Diwate, V. Ubale, R. Bhorkade and N. Maldar, *Int. J. Polym. Anal. Charact.*, 2021, **26**, 342–353.
22 A. L. Li, Z. C. Hao, C. Han and G. H. Cui, *Appl. Organomet. Chem.*, 2020, **34**(3), e5313.
23 Q. Q. Xiao, Y. H. Li, D. Liu and G. H. Cui, *Inorg. Chem. Commun.*, 2020, **111**, 107665.
24 A. L. Li, S. C. Wang, D. Liu and G. Y. Dong, *J. Solid State Chem.*, 2020, **290**, 121604.
25 G. Zhang and C. B. Musgrave, *J. Phys. Chem. A*, 2007, **111**, 1554–1561.
26 W. Humphrey, A. Dalke and K. Schulten, *J. Mol. Graphics*, 1996, **14**, 33–38.
27 Y. C. Kang, S. M. Treacy and T. Rovis, *ACS Catal.*, 2021, **11**, 7442–7449.
28 A. Cotic, I. Ramírez-Wierzbicki, G. E. Pieslinger, B. M. Aramburu-Trošelj and A. Cadranel, *Inorg. Chim. Acta*, 2021, **518**, 120246.
29 Y. S. Shi, D. Liu, L. Fu, Y. H. Li and G. Y. Dong, *CrystEngComm*, 2020, **22**, 4079–4093.
30 L. Shi, M. Liu and H. Li, *CrystEngComm*, 2020, **22**, 3753–3758.
31 Y. B. Wu, Q. Yu, G. H. Cui and L. Fu, *Transition Met. Chem.*, 2021, **46**, 1–14.
32 Y. S. Shi, Y. H. Li, G. H. Cui and G. Y. Dong, *CrystEngComm*, 2020, **22**, 905–914.
33 R. Das, G. Rajender and P. K. Giri, *Phys. Chem. Chem. Phys.*, 2018, **20**, 4527–4537.
34 F. Kafi, K. Jayathilaka, R. Wijesundera and W. Siripala, *J. Natl. Sci. Found. Sri Lanka*, 2021, **49**, 1.
35 Y. N. Wang, S. D. Wang, P. H. Dong, F. Wang, W. Q. Dou, S. Q. Lu, H. Q. Liu and K. Z. Cao, *Inorg. Chim. Acta*, 2021, **527**, 120546.
36 B. Zhu, Z. Zong, X. Zhang, D. Zhang, L. Cui, C. Bi and Y. Fan, *Appl. Organomet. Chem.*, 2020, **34**(7), e5518.
37 A. Ungordu and N. Tezer, *J. Mol. Graphics Modell.*, 2017, **74**, 265–272.
38 S. S. Li, Y. C. Zheng, X. M. Zhu, H. B. Wang, L. H. Liang, X. Z. Wang, L. Yuan, F. H. Zhang, H. Zheng and C. L. Zhao, *Sens. Actuators, B*, 2021, **337**, 129804.
39 A. L. Li, Z. C. Hao, C. Han and G. H. Cui, *Appl. Organomet. Chem.*, 2020, **34**, e5313.
40 H. Zhu, Y. H. Li, Q. Q. Xiao and G. H. Cui, *Polyhedron*, 2020, **187**, 114648.